Probing Atomic Distributions in Mono- and Bimetallic Nanoparticles by Supervised Machine Learning

Janis Timoshenko,[*,†] Cody J. Wrasman,[‡] Mathilde Luneau,[§] Tanya Shirman,[∥,⊥] Matteo Cargnello,[‡]
Simon R. Bare,[#] Joanna Aizenberg,[§,∥,⊥] Cynthia M. Friend,[§,∥] and Anatoly I. Frenkel[*,†,∇]

[†]Department of Materials Science and Chemical Engineering, Stony Brook University, Stony Brook, New York 11794, United States

[‡]Department of Chemical Engineering and SUNCAT Center for Interface Science and Catalysis, Stanford University, Stanford, California 94305, United States

[§]Department of Chemistry and Chemical Biology, [∥]John A. Paulson School of Engineering and Applied Sciences, and [⊥]Wyss Institute for Biologically Inspired Engineering, Harvard University, Cambridge, Massachusetts 02138, United States

[#]Stanford Synchrotron Radiation Lightsource, SLAC National Accelerator Laboratory, Menlo Park, California 94025, United States

[∇]Division of Chemistry, Brookhaven National Laboratory, Upton, New York 11973, United States

S Supporting Information

ABSTRACT: Properties of mono- and bimetallic metal nanoparticles (NPs) may depend strongly on their compositional, structural (or geometrical) attributes, and their atomic dynamics, all of which can be efficiently described by a partial radial distribution function (PRDF) of metal atoms. For NPs that are several nanometers in size, finite size effects may play a role in determining crystalline order, interatomic distances, and particle shape. Bimetallic NPs may also have different compositional distributions than bulk materials. These factors all render the determination of PRDFs challenging. Here extended X-ray absorption fine structure (EXAFS) spectroscopy, molecular dynamics simulations, and supervised machine learning (artificial neural-network) method are combined to extract PRDFs directly from experimental data. By applying this method to several systems of Pt and PdAu NPs, we demonstrate the finite size effects on the nearest neighbor distributions, bond dynamics, and alloying motifs in mono- and bimetallic particles and establish the generality of this approach.

KEYWORDS: Nanocatalysts, EXAFS, machine learning, neural network, molecular dynamics, bond length distribution
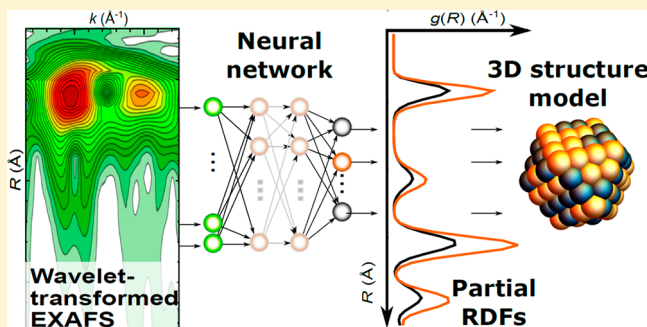
Architectures and compositional motifs of bimetallic nanoparticles (NPs) are diverse and tunable, which provides an opportunity for tailoring their properties, especially as heterogeneous catalysts.[1−8] The properties of such NPs are derived from their atomic arrangements and resultant electronic structure,[1,2,9−11] and thus depend strongly on particles composition, size, structure, and their dynamic behavior.[2,8,12−15] In addition to many challenges in NPs characterization in general,[16] bimetallic NPs in the size range of several nanometers or less pose an additional challenge of characterizing the distribution of the two components both on the surface and in the bulk.[17] Moreover, the structure, size, shape, and compositional motifs of a NP catalyst can change during the chemical reaction, therefore for studies of their catalytic mechanisms it is essential to characterize them in situ or in operando conditions.[2,10,18−21]

A convenient descriptor of atomic-scale structure in partially disordered materials (such as NPs) and/or materials experiencing structural transformations is a pair distribution function (PDF) or radial distribution function (RDF), which describe the real space, dynamic distribution of neighboring atoms. For multielement materials, such as nanoalloy A_xB_y, one can also define the partial radial distribution functions (PRDFs) that separately describe distributions of A and B atoms around a selected central atom. RDF and PRDF contain key information about the size of NP, its atomic structure, internal strain,[22,23] NP shape,[24] alloying motifs,[25−27] in situ restructuring and phase transitions,[28−32] atomic vibration dynamics,[33,34] interactions with support, ligands, and adsorbates.[35,36] Analysis of the electron, neutron and X-ray scattering data is a commonly used approach for extraction of the atomic pair distribution functions.[16,37] However, its applicability for bimetallic (and more complex) systems is limited due to the lack of chemical sensitivity.

An attractive approach for characterizing such multielement materials is the extraction of the PRDF data from the extended X-ray absorption fine structure (EXAFS) data.[38−42] Extraction of PRDF from the NP EXAFS, however, requires solving the

inverse problem, which is ill-defined,[43] and is especially problematic for ultrasmall NPs with strong surface-, ligand- and/or substrate- induced bond length asymmetry.[34,44–48] As a result, the commonly used EXAFS data-fitting method[49] is often limited to well-ordered materials and the first coordination shell only. The latter is a significant problem, because for the unambiguous characterization of NPs size, shape, and crystallographic structure (in the case of well-defined and monodispersed NPs), the access to more distant coordination shells is necessary.[42,50–55] For example, information from the more distant neighbors is needed to distinguish between crystalline and amorphous particles[56] or between close-packed and icosahedral atomic arrangements.[24] Also, the access to the distant coordination shells is necessary to discriminate between different alloying motifs. For example, a weak ordering of Pd and Au atoms was observed in thin films of PdAu[57–59] and experimental and theoretical studies reported the formation of various superstructures in bulk PdAu.[59,60] Moreover, theoretical studies of configurations of Pd atoms on bimetallic surfaces indicate that configurations consisting of first-neighbor Pd pairs are unstable, but that the formation of second-neighbor Pd ensembles is energetically favorable.[61,62] The presence of such structural motifs can clearly have an impact on the catalytic properties of bimetallic NPs, and tools are needed to detect them in experiment.

For disordered bulk materials with the known density, the PRDF can be extracted from EXAFS data using reverse Monte Carlo (RMC) simulations.[63–65] For nanomaterials, however, RMC is not immediately applicable, because the knowledge of the initial structure model (overall size, shape, and structure of the particle) is required.[47] We have also demonstrated[66] that useful insights into the relationship between the EXAFS features and NPs structural motifs can be obtained from classical molecular dynamics (MD), coupled with ab initio simulations of EXAFS spectra.[67] Recently we have shown that these insights can be turned into a powerful tool for an accurate RDF extraction, when MD-EXAFS method is coupled with supervised machine learning (artificial neural network (NN)) analysis. By employing NN, trained on theoretical MD-EXAFS data, we were able to reconstruct RDF in bulk iron across the structural phase transition.[30] Here we generalize this method to a large class of mono- and bimetallic NPs.

The great potential of this method is demonstrated by reconstructing PRDFs in well-defined PdAu nanoalloys, prepared via different techniques. This is a well understood system, relevant for many catalytic applications,[2,5,17,68–70] with a unique property that Pd and Au can form alloy within a broad range of compositions.[2] Thus, this system is ideally suited for this proof-of-principle work.

EXAFS Modeling in Multielement Materials. The particle-averaged EXAFS $\chi_A(k)$ of absorbing atom A (here k is the wavenumber for an X-ray excited photoelectron) can be expressed as a sum of contributions from all the possible photoelectron scattering paths, $\chi_A(k) = \sum_p \chi_{Ap}(k)$, including single-scattering (SS) and multiple-scattering (MS) contributions. In multielement materials, a SS contribution arising from the scattering from B-type atoms can be expressed as[71]

$$\chi_{AB}(k) = S_{0,A}^2 \int_0^{+\infty} F_{AB}(k, R) g_{AB}(R) \sin(2kR + \phi_{AB}(k, R)) \frac{dR}{kR^2}$$

(1)

Here $F_{AB}(k, R)$ and $\phi_{AB}(k,R)$ are scattering amplitude and phase functions that can be calculated theoretically and that

ensure chemical sensitivity of EXAFS (see Figure S1 in Supporting Information).[67] $S_{0,A}^2$ is the amplitude reduction factor due to many-electronic excitations that can be obtained from the analysis of reference materials. Finally, PRDF $g_{AB}(R)$ defines the distribution of the B-type atoms around atoms of the type A and encodes the information about the number of nearest neighbors of different types, interatomic distances, and disorder. The latter can be both due to thermal motion of atoms, as well as due to static deviations from the periodic lattice sites (e.g., due to a surface-induced strain in NPs). Importantly, because EXAFS is an averaging technique, $g_{AB}(R)$ accounts both for the interparticle and intraparticle variations in structural motifs, thus it can be quite complex in realistic nanostructured materials with many nonequivalent absorbing sites and in a common situation where NPs with different structures coexist.[72] Equation 1 can also be generalized to describe the MS contributions, by replacing $g_{AB}(R)$ with many-body distribution function and accounting for the dependencies of F and ϕ functions on the relative positions of scattering atoms.

Experimental EXAFS Data. Particle size and composition effects on EXAFS data are illustrated in Figure 1, where
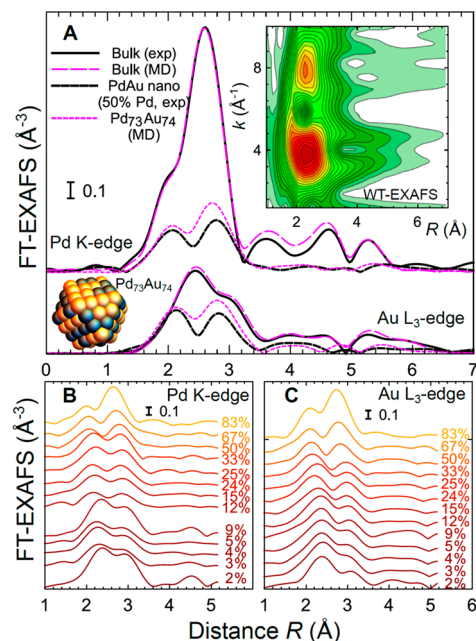
Figure 1. Fourier-transformed (FT) experimental[69] and simulated (with MD method[66]) Pd K-edge and Au L₃-edge EXAFS for bulk Au, Pd, and nanosized PdAu particles (50% Pd, peptide-templated synthesis) at room temperature (A). Snapshot of cuboctahedral PdAu NP obtained in MD simulations, and modulus of Morlet WT for experimental Pd K-edge data for PdAu NP are shown in the insets. Experimental Pd K-edge (B) and Au L₃-edge (C) EXAFS spectra for PdAu NPs with Pd concentration from 2 to 83%. Spectra are shifted vertically for clarity.

experimental Pd K-edge and Au L₃-edge EXAFS spectra for the PdAu alloy NPs with different Au to Pd ratios are shown and compared with the spectra for the bulk reference materials. Data for bimetallic NPs were obtained for a range of Pd concentrations and particle sizes, listed in Table 1. Table 1 and Figure 1 summarize previously published EXAFS data for R5 peptide-templated NPs with nominal Pd concentrations 25%, 33%, 50%, 67%, and 83% and NPs sizes (estimated by TEM)

**Table 1. Details of Bimetallic Samples, Investigated in This Study**

Pd concentration	average particle size (nm)	support/template
83%	3.0 ± 0.6	Peptide R5
67%	3.3 ± 0.7	Peptide R5
50%	3.4 ± 0.7	Peptide R5
33%	3.8 ± 0.7	Peptide R5
25%	4.0 ± 0.7	Peptide R5
24%	4.3 ± 0.8	TiO$_2$
15%	3.9 ± 0.6	TiO$_2$
12%	5.3 ± 0.4	TiO$_2$
5%	5.1 ± 0.4	TiO$_2$
4%	3.7 ± 0.7	TiO$_2$
3%	6.6 ± 0.6	TiO$_2$
9%	6.0 ± 2.1	SiO$_2$
2%	5.8 ± 1.4	SiO$_2$

from 3 to 4 nm,[69] as well as the original data for differently prepared samples, collected in two XAS experiments. PdAu NPs with the Pd concentrations of 4%, 15%, and 24% and sizes of about 4 nm and NPs with the Pd concentrations of 3%, 5%, and 12% and sizes of about 6 nm were prepared by seed-mediated colloidal synthesis method[73] and deposited on TiO$_2$. PdAu NPs with the Pd concentration of 2% and 9% and NPs sizes of about 5−6 nm were synthesized using sequential reduction method and incorporated into colloid-templated porous SiO$_2$ using previously published procedure.[74] Details of sample preparation and XAS measurements for these samples, TEM images, and results of conventional EXAFS data fitting are given in Supporting Information, Notes 1−2, Figures S2−S5, and Tables S1−S2. All particles are metallic, thus Pd K-edge and Au L$_3$-edge EXAFS spectra for these samples qualitatively resemble those of the bulk Au and Pd (Figure 1A). They have, however, significantly smaller amplitudes due to the particle size effect and structural and chemical disorder. Upon changes of Au to Pd ratio, all PRDFs $g_{Au-Pd}(R)$, $g_{Au-Au}(R)$, $g_{Pd-Pd}(R)$, $g_{Pd-Au}(R)$ are modified, resulting in the changes of the EXAFS spectra shown in Figure 1B,C. The observed trends in experimental spectra, however, are not immediately interpretable; homometallic and heterometallic contributions to the EXAFS spectra overlap completely, as do the contributions from the distant coordination shells and MS contributions. The interpretation of the Fourier-transformed

(FT) EXAFS spectra is further complicated by strong dependencies of the scattering functions F and ϕ on wavenumber k (Figure S1), characteristic for heavy metals.[75,76] To extract structural information from the EXAFS spectra, we rely here on the sensitivity of NNs to patterns and correlations in the analyzed spectra.[30,77,78]

Because the interpretation of the EXAFS spectra for bimetallic NPs is a challenging problem, before applying our procedure to PdAu NPs we validate it on a simpler example of monometallic particles. For this purpose, we revisit the temperature-dependent (160−573 K) EXAFS spectra for well-defined monometallic Pt NPs with sizes from 0.9 to 2.9 nm taken from ref 79. Pt NPs were prepared by the impregnation method and supported on γ-Al$_2$O$_3$ (see Supporting Information, Note 1).

Neural Network Construction and Training. Our NN is a composite function that takes as an input the experimental or simulated EXAFS data and provides as an output the PRDFs, approximated with a histogram between R_{min} = 1.92 Å and R_{max} = 6.00 Å; each output node of our NN yields a height of the corresponding histogram bin.[30] PRDFs for different atomic pairs (e.g., for Pd−Au and Pd−Pd) are obtained simultaneously; the NN output vector encodes concatenated interatomic distances histograms for both pairs. Data from different absorption edges (Pd K-edge and Au L$_3$-edge) are analyzed separately by individually trained NNs. During the training step, the NN parameters (weights) are optimized by requiring that for a large set of training EXAFS spectra the NN yields correct values of PRDFs. For such training, we use theoretical EXAFS data and the corresponding known PRDFs, obtained in classical MD simulations for a large set of PdAu random alloy NPs with different sizes, shapes, compositions, structures, and at different temperatures. The details of the MD simulations and ab initio EXAFS calculations are given in ref 66. As previously demonstrated[66] and shown in Figure 1, such MD simulations provide realistic-looking EXAFS spectra for bulk reference materials, as well as for a broad range of PdAu structures. As an example, in Figure 1A we compare with experimental data the Pd K-edge and Au L$_3$-edge MD-EXAFS spectra, calculated for bulk Pd and bulk Au at room temperature, as well as for PdAu NP. Also, as was shown before,[66] chemical sensitivity of EXAFS spectra in bimetallics can be improved by wavelet transform (WT) (see inset in
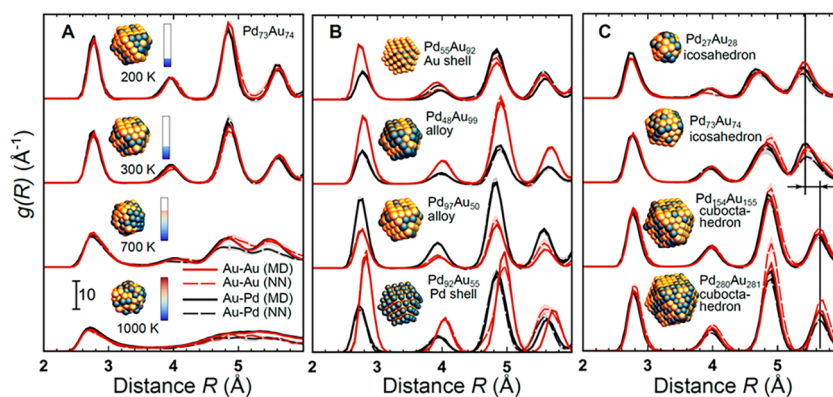

Figure 2. Validation of NN accuracy with theoretical data: Au−Au and Au−Pd PRDFs, yielded by NN from Au L$_3$-edge MD-EXAFS spectra are compared with the true PRDFs, calculated directly from MD coordinates for NPs at different temperatures (A) with different compositions (B) and sizes and crystallographic structures (C). In (A), all results correspond to cuboctahedral Pd$_{73}$Au$_{74}$ NP. For all cases in (B) and (C), the corresponding temperature is 300 K. PRDFs are shifted vertically for clarity.

Figure 1A). Therefore, before being processed by NN nodes, EXAFS spectra are mapped to (k,R)-space via complex Morlet WT.[30,80,81] Importantly, we deliberately limit our analysis to a relatively short-range in k-space, between 3 and 11 Å^{-1}, for which experimental EXAFS data of reasonable quality can usually be obtained for typical samples with low metal loading and in a broad range of reaction conditions The details of NN implementation and training are given in Supporting Information, Note 3 and Figures S6 and S7.

Neural Network Validation. To demonstrate the accuracy of our approach, we apply it first to the theoretical particle-averaged spectra obtained in MD-EXAFS calculations for the structure models discussed in ref 66. Note that these structures and their spectra were not used for the NN training. In Figure 2, we compare the PRDFs, obtained by the NN from such theoretical Au L$_3$-edge EXAFS data, with the true PRDFs, calculated from MD coordinates. Similar results obtained for Pd K-edge are shown in Supporting Information Figure S6. Figure 2 and Figure S6 also illustrate possible applications of this method. First, as shown in Figure 2A and Figure S6A, NN can reconstruct the complex, broad, and asymmetric PRDFs characteristic for NPs, especially at high temperatures. NN is also able to track the changes in the PRDFs upon changes in NPs composition and transition from a random alloy to a core–shell structure (Figure 2B and Figure S6B). The latter result is particularly remarkable because for our NN training we used data for random alloy particles only and yet the RDFs of core–shell NPs can also be recovered with a reasonable accuracy.

Finally, our NN is sensitive to the changes in the particle size and crystallographic structures (Figure 2C and Figure S6C). The difference between the PRDFs for these models is best seen in the contribution from the distant coordination shells. In particular, the third and fourth peak in PRDFs in the case of icosahedral atomic arrangement have comparable intensities, whereas the third peak is more pronounced in cuboctahedral NPs. Moreover, the fourth peak in the cuboctahedral NPs is shifted to larger interatomic distances, as shown in Figure 2C and Figure S6C. All these trends can be reproduced by our NN reliably.

Analysis of Experimental Data for Monometallic Systems. To further establish the validity of the NN approach discussed above, experimental data obtained for well-defined monometallic materials were analyzed first. In Figure 3, we show the RDFs, derived using the NN method for bulk Au and bulk Pd from the Au L$_3$-edge EXAFS for Au foil and Pd K-edge EXAFS for Pd foil. For these bulk materials, the results of the NN-EXAFS analysis are directly comparable with RMC results.[47,66] Such a comparison is also shown in Figure 3. In addition, as we demonstrated before,[30] due to the similarity of photoelectron scattering properties for atoms that are neighbors in the Periodic Table, we can apply the NN, trained on PdAu data, also to analyze EXAFS data from Rh, Ag, Pt, Ir metals, and their alloys. Therefore, in Figure 3 we apply our NN also to analyze the Pt L$_3$-edge EXAFS data in Pt foil and compare the obtained RDFs with the RMC results.[77] NN results agree very well with the RMC data and demonstrate the potential of our approach in detecting the differences in interatomic distances and disorder patterns in these bulk materials. Note that unlike our NN method, which (after training is completed) yields RDFs within seconds, RMC simulations require several CPU days, even for such simple systems as bulk metals.
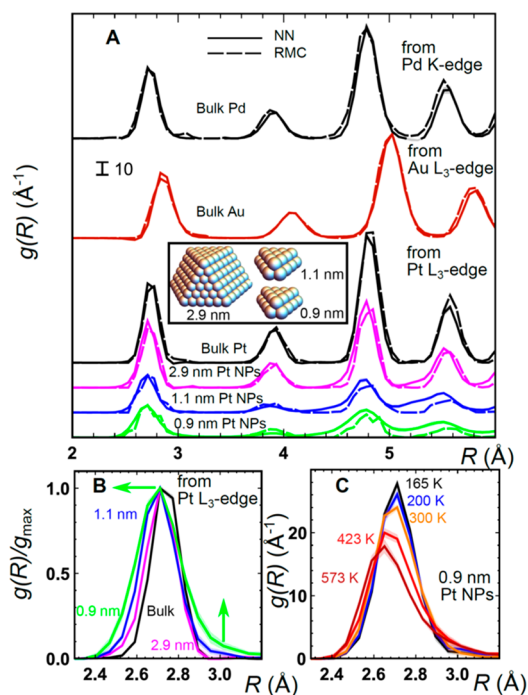
Figure 3. Reconstruction of RDF in monometallic compounds by NN method: RDFs obtained from Pd K-edge EXAFS for Pd foil, Au L$_3$-edge EXAFS for Au foil, Pt L$_3$-edge EXAFS for Pt foil, as well as from Pt L$_3$-edge EXAFS for Pt NPs with sizes 0.9, 1.1, and 2.9 nm.[79] For comparison, RDFs obtained independently from RMC simulations[47,66,77] are also shown (A). For Pt NPs to construct initial structure models (shown in the inset) required for RMC simulations, results of XANES analysis were used.[77] Normalized first shell RDFs for Pt NPs are shown in panel B. Temperature dependency of the first shell RDF, obtained by NN for 0.9 nm Pt NPs, is shown in panel C.

To explore sensitivity of our method to NPs size, it is further applied to the Pt L$_3$-edge EXAFS data in monometallic Pt NPs supported on γ-Al$_2$O$_3$[79] (Figure 3). Figure 3A,B shows the results, obtained from the room-temperature EXAFS data, whereas the results obtained from temperature-dependent EXAFS data are compared in Figure 3C (for the first coordination shell in 0.9 nm NPs) and Supporting Information, Figure S8 (for more distant coordination shells and 1.1 and 2.9 nm NPs). Our NN can detect clearly the differences in the RDFs for the NPs with TEM-determined sizes of 0.9, 1.1, and 2.9 nm; RDF peaks for smaller NPs are lower and broader, in agreement with the expected reduced coordination numbers (CNs) and enhanced disorder in these NPs. For 2.9 nm NPs, the position and intensity of the RDF peaks for the third and fourth coordination shells agree well with those for the face-centered cubic-type structure. For smaller particles, these peaks are significantly broadened and distorted, suggesting an onset of the deviations from the close-packed structure. These deviations are enhanced significantly upon the temperature increase (Figure S8).

The asymmetries of the RDFs for monometallic Pt NPs are best seen in Figure 3B. For clarity, we show here RDFs for the first coordination shell only and normalize RDFs for different NPs samples, dividing them by g_{max}, the maximal RDF value between 2.2 and 3.4 Å. The arrows in Figure 3B show two main trends in RDFs that are observed upon reduction of the NPs size. The first trend is the shift of the RDF peak to lower interatomic distances. It is expected for small NPs due to the
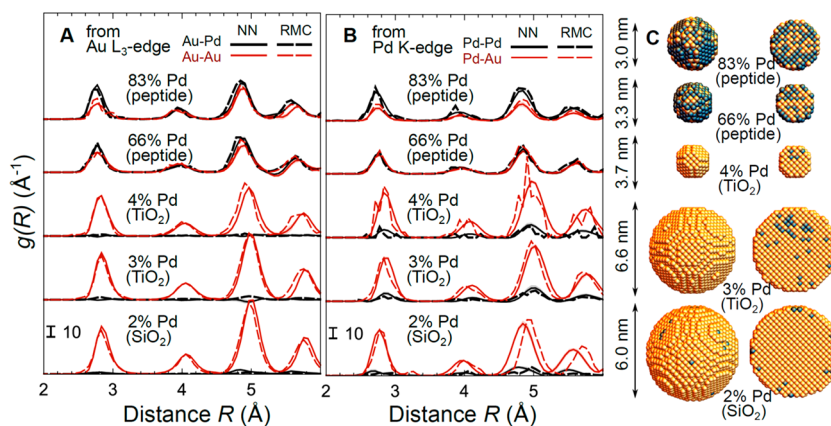
Figure 4. Reconstruction of PRDFs in bimetallic compounds by NN method: Au−Pd and Au−Au (A) and Pd−Pd and Pd−Au (B) PRDFs obtained from Au L₃-edge and Pd K-edge EXAFS for PdAu NPs with different Pd concentrations. The obtained PRDFs were integrated to obtain partial CNs, which were then used to construct possible 3D structure models, shown in panel C (3D models and their cuts are shown). Arrows (in scale) indicate the average NP sizes, as obtained by TEM. The obtained structure models were used as initial structure models for RMC simulations. PRDFs, obtained by RMC procedure, are compared with the original PRDFs yielded by NN in (A,B).

compression of interatomic distances by surface-induced tension.[45] The second trend is an increase of the RDF peak tail at larger R values, that is, the RDF peaks are positively skewed, and the skewness increases with the reduction in the NPs size. The two corresponding effects, responsible for the asymmetry of the RDFs in small NPs, are caused by the static and dynamic processes, respectively. The static effect is a result of the NP distortion because the outer atoms in NPs are more affected by the surface tension than the core atoms.[45,82] Upon reduction of the NPs size, the surface-to-volume ratio increases, thus one expects to observe an increase of the contribution from short bonds, and reduction of the contribution from the long bonds (increasingly negatively skewed RDFs).[45] The dynamic effect is revealed in the elongation of metal−metal bonds due to strong anharmonicity of the atomic thermal motion, which is especially pronounced for surface atoms.[32] Because of this anharmonic effect, the contribution of longer bonds is expected to increase with the reduction of the NPs size, resulting in increasingly positively skewed RDFs. As one can see from Figure 3B, for supported Pt NPs at room temperature dynamic effects dominate over static effects. In fact, despite the shift of the RDF maxima to lower R values due to the surface tension, the contribution of the long Pt−Pt bonds in small NPs is significantly larger than in larger NPs, which may have important implications for cases where NP properties (e.g., adsorption energies for different adsorbates) depend on interatomic distances. The anharmonicity of atomic motion and the associated positive RDF skewness are enhanced upon temperature increase (Figure 3C). However, even at the lowest available temperature (165 K) the dynamic effects dominate over static distortions and RDF peak remains positively skewed. As an additional check, the maxima of RDF peaks are shifted to the lower interatomic distances as temperature increases (Figure 3C), in agreement with the previously reported negative thermal expansion, observed in supported Pt NPs in conventional EXAFS fitting.[79]

For comparison, we show in Figure 3A also the results of RMC-EXAFS simulations for Pt NPs, where the initial structure model, required for RMC method, was estimated based on the X-ray absorption near edge structure (XANES) analysis.[77] NN and independently obtained RMC results are in an excellent agreement, which demonstrates clearly the ability

of the NN-EXAFS approach to reconstruct reliably the asymmetric, non-Gaussian shapes of RDFs, characteristic for small NPs.

Analysis of Experimental Data for Bimetallic Nanoparticles. Application of the NN approach to interpret EXAFS data for bimetallic PdAu NPs with different sizes and Pd-to-Au ratios and prepared via different synthesis methods, demonstrates the success of this method in more complex systems. All materials studied have four distinct peaks in PRDFs between R_{min} and R_{max}, consistent with the close-packed structure (Figure 4A), both in the Au−Pd and Au−Au PRDFs reconstructed from the Au L₃-edge EXAFS (Figure 4A), and in the Pd−Au and Pd−Pd PRDFs reconstructed from the Pd K-edge EXAFS (Figure 4B). The shape of all peaks, however, deviates notably from a Gaussian, indicating that the conventional EXAFS data fitting should be used with caution for these systems.

For particles of different sizes and similar Pd concentrations, the intensity of PRDF features correlates well with the NPs' size, as obtained from TEM (Figure 4C), in that that there is an increase in average CNs for larger particles. For NPs with different Pd concentrations, there is also a clear correlation between the Pd concentration and the relative intensity of the Au−Pd and Au−Au PRDFs (Figure 4A) and Pd−Pd and Pd−Pd PRDFs (Figure 4B): for Au-rich particles, Au−Au and Pd−Au contributions dominate. This observation is in agreement with the expected random alloy structure of all investigated particles. The peaks of the obtained PRDFs show a shift to smaller R values upon increase of Pd concentration, in agreement with Vegard's law for alloys and the fact that the lattice constant for Pd (3.891 Å) is smaller than that for Au (4.080 Å).[83] An interesting deviation from this systematic behavior here is Pd−Au PRDF in the PdAu NPs, which have the smallest Pd concentration. In particular, PdAu particles, embedded in SiO₂, have similar Pd concentrations and particle sizes as those on TiO₂, yet their Pd−Au PRDF peaks seem to be shifted to slightly lower interatomic distances. The positions of the Au−Au peaks for these NPs, however, follow Vegard's law. One possible explanation for this deviation is segregation of Pd atoms to the particle surface, where interatomic distances are shortened by tensile stress.[45]

To understand the distribution of atoms within NPs in more details and for more quantitative analysis, we integrate the found RDFs to obtain partial CNs[30]

$$C_{i,AB} = \int_{R_{i-1,AB}}^{R_{i,AB}} g_{AB}(R)\mathrm{d}R \qquad (2)$$

and average interatomic distances

$$\langle R \rangle_{i,AB} = \frac{1}{C_{i,AB}} \int_{R_{i-1,AB}}^{R_{i,AB}} g_{AB}(R)R \ \mathrm{d}R \qquad (3)$$

In both cases the integration is carried out between $R_{i-1,AB}$ and $R_{i,AB}$ corresponding to $(i-1)$th and ith minima of PRDF $g_{AB}(R)$. Higher moments of the bond-length distribution can be obtained similarly. The resulting CNs and interatomic distances are reported in Figure 5 and in Supporting
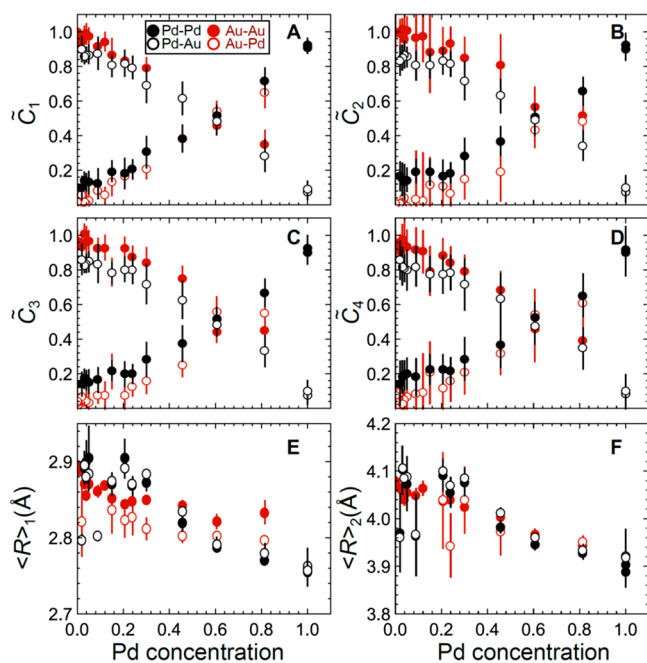
Figure 5. Concentration dependencies of the normalized coordination numbers $\tilde{C}_1$, $\tilde{C}_2$, $\tilde{C}_3$, and $\tilde{C}_4$ for the first four coordination shells (A−D) and average interatomic distances R for the first two coordination shells (E,F) obtained by integration of PRDFs, extracted by NN from experimental EXAFS data.

Information, Table S3. CNs for the first coordination shell, in principle, can be compared with those from the conventional EXAFS analysis but, as mentioned previously, such a comparison should be taken with caution due to the known artifacts in the conventional EXAFS fitting procedure. Nevertheless, as we demonstrate in Supporting Information, Figure S9, in this particular case the CNs obtained by the NN method and via conventional EXAFS fitting agree well. Importantly, even for samples where conventional EXAFS fitting shows a small contribution of Pd—O bonds (see Table S1 in Supporting Information), the metal−metal CNs yielded by our NN (which was not trained to recognize oxide contribution) seem to be reliable.

For an additional validation of the obtained results, we plot in Figure 5A−D the obtained partial CNs for the first four coordination shells as a function of the Pd concentration. To compensate for the difference in the NPs size, CNs in Figure 5

are normalized by dividing them by the total coordination number for corresponding metal: $C_{i,Pd} = C_{i,Pd-Au} + C_{1,Pd-Pd}$ for Pd and $C_{i,Au} = C_{i,Au-Au} + C_{i,Au-Pd}$ for Au. The slopes of functions that show the dependency of normalized CNs $\tilde{C}_{i,AB}$ for A−B atomic pair for the ith coordination shell on the concentration of metal x_B can be directly linked to Cowley's short-range order parameter[41,52]

$$\alpha_{i,AB} = 1 - \frac{C_{i,AB}}{(C_{i,AB} + C_{i,AA})x_B} = 1 - \frac{\tilde{C}_{i,AB}}{x_B} \qquad (4)$$

In perfect random PdAu alloy structure (all $\alpha_i = 0$) the normalized CNs should linearly change from 0 to 1 or from 1 to 0 upon increase of Pd concentration. This trend for the first coordination shell can be clearly seen in Figure 5A. Importantly, using NN method we can extend for the first time this analysis beyond the first coordination shell, which is important for a more detailed analysis of structural motifs.[60] In this particular case, we observe that Pd and Au atoms are distributed stochastically in all four coordination shells (Figure 5A−D), which demonstrates the accuracy of the obtained PRDFs up to 6 Å.

Concentration dependencies of the average interatomic distances R for the first two coordination shells are shown in Figure 5E,F. The resolution of our method in R-space is limited by the short k-range used for the analysis ($k_{max} = 11$ Å^{-1}) and the finite width of the histogram bin used for the PRDF parametrization (0.06 Å in our case). Nevertheless, one can see that, in agreement with the results of visual examination of PRDFs and in agreement with Vegard's law, all interatomic distances decrease upon the increase of Pd concentration. Here, for the first time this effect is demonstrated in nanoalloys for not only the first coordination shell (Figure 5E) but also for more distant shells (Figure 5F). It is interesting to note that while Vegard's law predicts that concentration dependencies for the Pd—Pd, Pd—Au, and Au—Au distances should be the same, our results show that it is not the case, and one can note that the Au—Au bond is compressed less upon increase of Pd concentration than the Pd—Pd bond. Previously, a similar effect was observed in CuAu bulk alloys,[84] and it was attributed to the asymmetry of interatomic interaction potential: because the repulsive interaction between atoms is more sensitive to the changes in interatomic distances than attractive interaction, the bond between larger atoms (Au) is stiffer than the bond between smaller atoms (Cu, or, in our case, Pd) for metal alloys formed by atoms with different sizes.[84] According to this argument, this effect should be observed only for the first nearest neighbors. Indeed, as shown in Figure 5F, the concentration dependencies for the Pd—Pd and Au—Au bonds are almost the same for the second coordination shell. In addition, both for the first and second coordination shells deviations from Vegard's law showing unexpectedly short bond lengths for Pd—Au atomic pairs are observed for some samples with very low Pd concentration, in agreement with the results, presented in Figure 4. As we mentioned above, one possible explanation for these outliers is the segregation of Pd to NP surface.

Nanoparticle 3D Structure Modeling. Using the obtained CNs values, we can construct 3D structure models of the investigated particles (Figure 4C) using an iterative optimization procedure, as described in Supporting Information, Note 4. One should emphasize here that the interpretation of the CNs in terms of a single particle model

requires caution, because experimental spectra (and, hence, PRDFs and CNs, yielded by NN) are averaged over many NPs in the sample, which may have different sizes, shapes, and compositions. For samples with a broad distribution of particle sizes and compositions, such analysis can be misleading.[41,42] In our case, narrow distributions of NP sizes and compositions were controlled by the chosen synthesis methods and verified by electron microscopy techniques.

As shown in Table S3 in Supporting Information, for all samples, all 16 partial CNs, calculated for the model NPs, are in a good agreement with the CNs obtained from the NN analysis. It gives us confidence in the obtained structure models. The concentrations of Pd and Au atoms in the models in Figure 4C correlate well with the nominal concentrations. The size of the best model particles matches well the average particle sizes from the TEM measurements (Figure 4C). This analysis thus resolves one of the controversies of our previous work,[66] where we have analyzed spectra of the same peptide-templated PdAu particles as here, but instead of using NN we attempted to directly match the experimental EXAFS data with the simulated spectra for different MD models. In that previous study, the best agreement was obtained for the model particles with size about 1.5 nm, which was noticeably smaller than the result of the TEM measurements. This difference can be attributed to systematic errors of the MD modeling due to the inaccuracies of the employed interaction models. As one can see, by using the NN approach where we do not rely explicitly on the accuracy of MD models, much better agreement with the experimental TEM data can be obtained.

In samples with larger concentration of Pd, the distribution on Pd and Au atoms seems to be quasi-random. For the sample embedded in SiO_2, however, the structure model in Figure 4C points strongly toward the segregation of Pd to the surface. This trend can be traced back to the NN-yielded CNs values, as summarized in Table S3 in Supporting Information; note that Pd—Au CNs for all coordination shells in this sample are smaller than corresponding Au—Au CNs, suggesting the presence of a large fraction of undercoordinated Pd atoms. While by its own this observation can be dismissed as an artifact of our new method, it is noteworthy that it is the same sample for which we already proposed that the segregation of Pd atoms to the particle surface is a possible explanation of the observed anomalies in Pd—Au distances. Thus, two independently obtained quantities (CNs and interatomic distances) both point to the same conclusion. Note that there are numerous reports that interactions of Pd with adsorbates (CO or O_2) can indeed result in Pd-enriched surface in PdAu alloys.[70,85−90] More systematic analysis of this effect in NPs with low Pd concentration deserves a separate study.

For an additional validation of these structure models, we rely on RMC simulations.[47,65,66] The models, shown in Figure 4C, were further optimized by allowing small atomic displacements but preserving particle size, shape, and distribution of atoms within NP with the aim to minimize the difference between the experimental and simulated EXAFS spectra. RMC simulations were carried out as in ref 66. The advantage of RMC simulations is that they allow us to directly compare theoretical EXAFS spectra calculated for particle models (in this case, constructed based on the NN analysis) with the original experimental EXAFS data and thus to confirm and quantify the agreement between the theoretical structure models and experimental results. Such information, which is critical for assessing the reliability of the analysis, is challenging to extract from the NN results only.

The final structure models and the good final agreement between experimental and theoretical spectra are demonstrated in Supporting Information, Figure S10. To verify that PRDFs in the models, obtained in RMC simulations, are the same as the original PRDFs, yielded by NN, we compare them in Figure 4A,B, and obtain a good agreement for all samples. The only noticeable deviation is obtained for Pd K-edge data in 2% Pd NP on SiO_2, where for the third and fourth coordination shells Pd—Au RDF peaks are shifted to slightly larger R values in RMC results. We attribute this difference to an artifact of RMC rather than NN procedure; note that the structure model for this particle contains more than 7000 atoms, and it is challenging to obtain a perfectly converged solution for the system with so many degrees of freedom in RMC simulations, where both the complexity of problems (the number of required iterations) and the required computational time per iteration scale nonlinearly with the number of atoms. An indication that the obtained RMC solution is not optimal can be seen in Figure S10, where for Pd K-edge for this system a noticeably larger deviation between experimental and theoretical spectra can be observed in the R-range between 4 and 7 Å than in other cases. In addition, the contribution of the third and fourth coordination shells to the total EXAFS is relatively weak, thus it is not surprising that, while NN and RMC methods agree well for this sample for the first two coordination shells, larger deviations are observed in the contributions of more distant atoms.

New Insights in NPs Properties Enabled by NN-Based Approach. To summarize, the NN-based method for the extraction of PRDFs from the experimental EXAFS provides unique new information about the properties of mono- and bimetallic particles that would be challenging or impossible to obtain using a conventional EXAFS fitting approach. The extraction of the shapes of PRDF peaks, provided by the NN method, allows us to quantitatively compare static and dynamic contributions to the NPs structure and anharmonic effects in atomic motion, as demonstrated for the Pt nanoparticles.

As we demonstrated, the contributions of more distant coordination shells enable an accurate determination of structural and alloying motifs in metallic NPs. In particular, access to distant coordination shells is required to detect deviations from the close-packed structure (as observed here for Pt nanoparticles) and to identify more subtle fingerprints of ordering in alloys, such as second-neighbor ensembles. For the first time, we have shown that based on the EXAFS data one can use the Cowley's relationship (eq 4) to characterize distributions of atoms beyond the first-neighbor pairs and that in the particular case of PdAu nanoalloys Pd and Au atoms remain stochastically distributed within all four nearest coordination shells.

Moreover, by comparing interatomic distances between different types of atoms in the first and more distant coordination shells we were able to get more detailed understanding of local structure relaxation processes due to atomic size mismatch in random alloys. In particular, we observed that the homometallic bond between larger (Au) atoms in the first coordination shells is less affected by the changes in Pd concentration than predicted by Vegard's law but no such deviations are present for the second coordination shell. We attribute this effect to the asymmetry of the

interatomic interaction potential, which makes close-packed Au—Au pairs less affected by the presence of Pd atoms. Such information will be useful for future developments of interatomic potential models for alloys, which is a challenging task.[91,92]

Finally, in a special case of NPs with well-defined particle size and compositional distributions, the CNs yielded by the NN can be employed to construct a complete 3D structure model. Access to the CNs from distant coordination shells is, again, essential for this purpose due to the enhanced sensitivity of these CNs to particle geometry.[42,50−54] In this work, we used this approach to construct 3D models of various PdAu NPs, and we have found them in a good agreement with the available, independently obtained information on particle sizes and compositions. In most cases, a random distribution of Pd and Au atoms within NP was observed. Intriguingly, for one group of PdAu NPs with low Pd concentration that were embedded in SiO_2, the obtained 3D structure model indicates segregation of Pd to NPs surface. This segregation trend (predicted also by theoretical models)[85−90] was indirectly confirmed also by the analysis of interatomic distances. Although this effect requires more systematic investigation, it illustrates well the power of our method.

We emphasize here that if the NPs size/compositional distribution is not narrow, the analysis of particle 3D shape, as presented here, would yield only an averaged, effective NP model. Analysis of this model (and its in situ evolution) still may be useful for understanding the NPs' properties[93] but needs to be carried out with extra caution. We emphasize, however, that for ensembles of small, well-defined clusters, where the PRDFs for each individual cluster are unique and known, our method can provide the distribution of clusters of different types, by analyzing and decomposing the ensemble-averaged PRDFs, yielded by the NN-EXAFS analysis.

To conclude, using a set of theoretical and experimental EXAFS spectra for well-defined mono- and bimetallic NPs with narrow size and compositional distributions, we have demonstrated that the information about the short and medium-range real-space distributions of atoms around absorbing metal species can be reliably extracted from the EXAFS data in multielement and/or nanoscaled materials. The parameter-free approach for the description of bond-length distributions, implemented in the NN-EXAFS method, allows us to probe asymmetric, non-Gaussian distributions of bond lengths, characteristic for small distorted metal NPs, as well as for thermal disorder effects in materials at high temperatures. The ability of our method to recognize contributions beyond the first nearest neighbors, in turn, allows us for the first time to carry out advanced analysis of alloying motifs in distant coordination shells both in bulk and nanoalloys and, for samples with well-defined NPs size and compositional distributions, to benefit from the sensitivity of these contributions to NPs morphology for the accurate determination of the 3D structure model of mono- and bimetallic nanoparticles. This information is important for establishing structure−properties relationship in many types of functional materials. Importantly, our approach does not rely on the EXAFS data of exceptionally high quality, as we demonstrate here by using the spectra with quite short k-range (up to 11 $Å^{-1}$ only); thus, it can be applied not only to model systems but to a broad range of in situ investigations of realistic nanomaterials and bulk alloys, relevant, e.g., for applications in catalysis. Because the NN-EXAFS method employs indirectly information from MD simulations (used for NN training), it can help to constrain the solution to be physically reasonable, even if there is not enough information in experimental EXAFS spectra due to limited k-range. The NN-based analysis of EXAFS data is also very quick (after training is completed), allowing one to extract the information about the material structure in real time; thus it is attractive for high-throughput and "on-the-fly" analysis. We believe that our approach can be easily generalized to many other systems, including non-metallic materials.

■ ASSOCIATED CONTENT

Ⓢ Supporting Information

The Supporting Information is available free of charge on the [ACS Publications website](#) at DOI: [10.1021/acs.nanolett.8b04461](#).

> Photoelectron scattering amplitudes and phases in PdAu particles, details of sample preparation and experimental characterization, TEM images for PdAu NPs on TiO_2 and in SiO_2, conventional EXAFS analysis for PdAu NPs on TiO_2 and in SiO_2, fitting results and obtained structure parameters, details of neural network implementation and training, validation of NN accuracy with theoretical data for Pd K-edge, dependences of training error, validation error and experimental error on the number of training examples, validation of NN accuracy with experimental data, details of NP 3D structure modeling, partial CNs obtained by NN-method from experimental EXAFS data and CNs for corresponding model particle, validation of structure models, obtained from NN-EXAFS analysis, with RMC-EXAFS method ([PDF](#))

■ AUTHOR INFORMATION

Corresponding Authors

*E-mail: Janis.timoshenko@gmail.com.
*E-mail: anatoly.frenkel@stonybrook.edu. Phone: +1 631-632-2751. Fax: +1 631-632-8052.

ORCID Ⓞ

Matteo Cargnello: 0000-0002-7344-9031
Simon R. Bare: 0000-0002-4932-0342
Cynthia M. Friend: 0000-0002-8673-9046
Anatoly I. Frenkel: 0000-0002-5451-1207

Notes

The authors declare no competing financial interest.

■ REFERENCES

(1) Liu, P.; Nørskov, J. K. *Phys. Chem. Chem. Phys.* **2001**, *3* (17), 3814−3818.

(2) Gao, F.; Goodman, D. W. *Chem. Soc. Rev.* **2012**, *41* (24), 8009−8020.

(3) Peng, X.; Pan, Q.; Rempel, G. L. *Chem. Soc. Rev.* **2008**, *37* (8), 1619−1628.

(4) Chen, P.-C.; Liu, X.; Hedrick, J. L.; Xie, Z.; Wang, S.; Lin, Q.-Y.; Hersam, M. C.; Dravid, V. P.; Mirkin, C. A. *Science* **2016**, *352* (6293), 1565−1569.

(5) Agarwal, N.; Freakley, S. J.; McVicker, R. U.; Althahban, S. M.; Dimitratos, N.; He, Q.; Morgan, D. J.; Jenkins, R. L.; Willock, D. J.; Taylor, S. H.; et al. *Science* **2017**, *358* (6360), 223−227.

(6) Wong, A.; Liu, Q.; Griffin, S.; Nicholls, A.; Regalbuto, J. *Science* **2017**, *358* (6369), 1427−1430.

(7) Hwang, B.-J.; Sarma, L. S.; Chen, J.-M.; Chen, C.-H.; Shih, S.-C.; Wang, G.-R.; Liu, D.-G.; Lee, J.-F.; Tang, M.-T. *J. Am. Chem. Soc.* **2005**, *127* (31), 11140−11145.

(8) Kim, D.; Resasco, J.; Yu, Y.; Asiri, A. M.; Yang, P.; et al. *Nat. Commun.* **2014**, *5*, 4948.

(9) Burch, R. *Acc. Chem. Res.* **1982**, *15* (1), 24−31.

(10) Tao, F. F. *Chem. Soc. Rev.* **2012**, *41* (24), 7977−7979.

(11) Ulissi, Z. W.; Tang, M. T.; Xiao, J.; Liu, X.; Torelli, D. A.; Karamad, M.; Cummins, K.; Hahn, C.; Lewis, N. S.; Jaramillo, T. F.; et al. *ACS Catal.* **2017**, *7* (10), 6600−6608.

(12) Norskov, J. K.; Bligaard, T.; Rossmeisl, J.; Christensen, C. H. *Nat. Chem.* **2009**, *1* (1), 37−46.

(13) Seh, Z. W.; Kibsgaard, J.; Dickens, C. F.; Chorkendorff, I.; Nørskov, J. K.; Jaramillo, T. F. *Science* **2017**, *355* (6321), No. eaad4998.

(14) Somorjai, G. A.; Park, J. Y. *Top. Catal.* **2008**, *49* (3−4), 126−135.

(15) Bu, L.; Zhang, N.; Guo, S.; Zhang, X.; Li, J.; Yao, J.; Wu, T.; Lu, G.; Ma, J.-Y.; Su, D.; et al. *Science* **2016**, *354* (6318), 1410−1414.

(16) Billinge, S. J. L.; Levin, I. *Science* **2007**, *316* (5824), 561−565.

(17) Weir, M. G.; Knecht, M. R.; Frenkel, A. I.; Crooks, R. M. *Langmuir* **2010**, *26* (2), 1137−1146.

(18) Divins, N. J.; Angurell, I.; Escudero, C.; Pérez-Dieste, V.; Llorca, J. *Science* **2014**, *346* (6209), 620−623.

(19) Tao, F.; Grass, M. E.; Zhang, Y.; Butcher, D. R.; Renzas, J. R.; Liu, Z.; Chung, J. Y.; Mun, B. S.; Salmeron, M.; Somorjai, G. A. *Science* **2008**, *322* (5903), 932−934.

(20) Tupy, S. A.; Karim, A. M.; Bagia, C.; Deng, W.; Huang, Y.; Vlachos, D. G.; Chen, J. G. *ACS Catal.* **2012**, *2* (11), 2290−2296.

(21) Hejral, U.; Franz, D.; Volkov, S.; Francoual, S.; Strempfer, J.; Stierle, A. *Phys. Rev. Lett.* **2018**, *120* (12), 126101.

(22) Masadeh, A.; Božin, E.; Farrow, C.; Paglia, G.; Juhas, P.; Billinge, S.; Karkamkar, A.; Kanatzidis, M. *Phys. Rev. B: Condens. Matter Mater. Phys.* **2007**, *76* (11), 115413.

(23) Gilbert, B. *J. Appl. Crystallogr.* **2008**, *41* (3), 554−562.

(24) Glasner, D.; Frenkel, A. I. *AIP Conf. Proc.* **2006**, *882* (1), 746−748.

(25) Calvo, F.; Cottancin, E.; Broyer, M. *Phys. Rev. B: Condens. Matter Mater. Phys.* **2008**, *77* (12), 121406.

(26) Chung, J. S.; Thorpe, M. *Phys. Rev. B: Condens. Matter Mater. Phys.* **1997**, *55* (3), 1545.

(27) Petkov, V.; Shastri, S.; Kim, J.-W.; Shan, S.; Luo, J.; Wu, J.; Zhong, C.-J. *Acta Crystallogr., Sect. A: Found. Adv.* **2018**, *74* (5), 553−566.

(28) Billinge, S.; Kwei, G. *J. Phys. Chem. Solids* **1996**, *57* (10), 1457−1464.

(29) Katayama, Y.; Mizutani, T.; Utsumi, W.; Shimomura, O.; Yamakata, M.; Funakoshi, K.-i. *Nature* **2000**, *403* (6766), 170.

(30) Timoshenko, J.; Anspoks, A.; Cintins, A.; Kuzmin, A.; Purans, J.; Frenkel, A. I. *Phys. Rev. Lett.* **2018**, *120* (22), 225502.

(31) Newton, M. A.; Chapman, K. W.; Thompsett, D.; Chupas, P. J. *J. Am. Chem. Soc.* **2012**, *134* (11), 5036−5039.

(32) Hu, W.; Xiao, S.; Yang, J.; Zhang, Z. *Eur. Phys. J. B* **2005**, *45* (4), 547−554.

(33) Jeong, I.-K.; Heffner, R.; Graf, M.; Billinge, S. *Phys. Rev. B: Condens. Matter Mater. Phys.* **2003**, *67* (10), 104301.

(34) Clausen, B. S.; Norskov, J. K. *Top. Catal.* **2000**, *10* (3−4), 221−230.

(35) Yancey, D. F.; Chill, S. T.; Zhang, L.; Frenkel, A. I.; Henkelman, G.; Crooks, R. M. *Chem. Sci.* **2013**, *4* (7), 2912−2921.

(36) Wang, L.-L.; Khare, S. V.; Chirita, V.; Johnson, D. D.; Rockett, A. A.; Frenkel, A. I.; Mack, N. H.; Nuzzo, R. G. *J. Am. Chem. Soc.* **2006**, *128* (1), 131−142.

(37) Egami, T.; Billinge, S. J. *Underneath the Bragg peaks: structural analysis of complex materials*; Pergamon: Amsterdam, 2012.

(38) Rehr, J. J.; Albers, R. C. *Rev. Mod. Phys.* **2000**, *72* (3), 621−654.

(39) Sinfelt, J.; Via, G.; Lytle, F. *Catal. Rev.: Sci. Eng.* **1984**, *26* (1), 81−140.

(40) Sinfelt, J.; Via, G.; Lytle, F. *J. Chem. Phys.* **1980**, *72* (9), 4832−4844.

(41) Frenkel, A. I. *Chem. Soc. Rev.* **2012**, *41* (24), 8163−8178.

(42) Frenkel, A. I.; Yevick, A.; Cooper, C.; Vasic, R. *Annu. Rev. Anal. Chem.* **2011**, *4*, 23−39.

(43) Babanov, Y. A.; Vasin, V.; Ageev, A. L.; Ershov, N. *Phys. Status Solidi B* **1981**, *105* (2), 747−754.

(44) Clausen, B. S.; Topsøe, H.; Hansen, L. B.; Stoltze, P.; Nørskov, J. K. *Jpn. J. Appl. Phys.* **1993**, *32* (S2), 95−97.

(45) Yevick, A.; Frenkel, A. I. *Phys. Rev. B: Condens. Matter Mater. Phys.* **2010**, *81* (11), 115451.

(46) Chill, S. T.; Anderson, R. M.; Yancey, D. F.; Frenkel, A. I.; Crooks, R. M.; Henkelman, G. *ACS Nano* **2015**, *9* (4), 4036−4042.

(47) Timoshenko, J.; Frenkel, A. I. *Catal. Today* **2017**, *280*, 274−282.

(48) Crozier ED, R. J.; Ingalls, R. Amorphous and liquid systems. In *X-ray absorption: principles, applications, techniques of EXAFS, SEXAFS, and XANES*; Koningsberger, D., Prins, R., Eds.; John Wiley and Sons: New York, 1988; p 373.

(49) Bunker, G. *Nucl. Instrum. Methods Phys. Res.* **1983**, *207* (3), 437−444.

(50) Jentys, A. *Phys. Chem. Chem. Phys.* **1999**, *1* (17), 4059−4063.

(51) Frenkel, A. I. *J. Synchrotron Radiat.* **1999**, *6*, 293−295.

(52) Frenkel, A. *Z. Kristallogr. - Cryst. Mater.* **2007**, *222* (11), 605−611.

(53) Mostafa, S.; Behafarid, F.; Croy, J. R.; Ono, L. K.; Li, L.; Yang, J. C.; Frenkel, A. I.; Cuenya, B. R. *J. Am. Chem. Soc.* **2010**, *132* (44), 15714−15719.

(54) Frenkel, A. I.; Hills, C. W.; Nuzzo, R. G. *J. Phys. Chem. B* **2001**, *105* (51), 12689−12703.

(55) Timoshenko, J.; Roese, S.; Hövel, H.; Frenkel, A. I. *Radiat. Phys. Chem.* **2018**, DOI: 10.1016/j.radphyschem.2018.11.003

(56) Li, L.; Wang, L.-L.; Johnson, D. D.; Zhang, Z.; Sanchez, S. I.; Kang, J. H.; Nuzzo, R. G.; Wang, Q.; Frenkel, A. I.; Li, J.; et al. *J. Am. Chem. Soc.* **2013**, *135* (35), 13062−13072.

(57) Nagasawa, A.; Matsuo, Y.; Kakinoki, J. *J. Phys. Soc. Jpn.* **1965**, *20* (10), 1881−1885.

(58) Matsuo, Y.; Nagasawa, A.; Kakinoki, J. *J. Phys. Soc. Jpn.* **1966**, *21* (12), 2633−2637.

(59) Schönfeld, B.; Sax, C. R.; Ruban, A. V. *Phys. Rev. B: Condens. Matter Mater. Phys.* **2012**, *85* (1), 014204.

(60) Atanasov, I.; Hou, M. *Surf. Sci.* **2009**, *603* (16), 2639−2651.

(61) Yuan, D.; Gong, X.; Wu, R. *Phys. Rev. B: Condens. Matter Mater. Phys.* **2007**, *75* (8), 085428.

(62) Gotsis, H.; Rivalta, I.; Sicilia, E.; Russo, N. *Chem. Phys. Lett.* **2009**, *468* (4−6), 162−165.

(63) Gurman, S.; McGreevy, R. *J. Phys.: Condens. Matter* **1990**, *2* (48), 9463.

(64) Luo, W.; Sheng, H.; Alamgir, F.; Bai, J.; He, J.; Ma, E. *Phys. Rev. Lett.* **2004**, *92* (14), 145502.

(65) Timoshenko, J.; Kuzmin, A.; Purans, J. *J. Phys.: Condens. Matter* **2014**, *26* (5), 055401.

(66) Timoshenko, J.; Keller, K. R.; Frenkel, A. I. *J. Chem. Phys.* **2017**, *146* (11), 114201.

(67) Ankudinov, A. L.; Ravel, B.; Rehr, J. J.; Conradson, S. D. *Phys. Rev. B: Condens. Matter Mater. Phys.* **1998**, *58* (12), 7565−7576.

(68) Bedford, N. M.; Showalter, A. R.; Woehl, T. J.; Hughes, Z. E.; Lee, S.; Reinhart, B.; Ertem, S. P.; Coughlin, E. B.; Ren, Y.; Walsh, T. R.; et al. *ACS Nano* **2016**, *10* (9), 8645−8659.

(69) Merrill, N. A.; McKee, E. M.; Merino, K. C.; Drummy, L. F.; Lee, S.; Reinhart, B.; Ren, Y.; Frenkel, A. I.; Naik, R. R.; Bedford, N. M.; et al. *ACS Nano* **2015**, *9* (12), 11968−11979.

(70) Wrasman, C. J.; Boubnov, A.; Riscoe, A. R.; Hoffman, A. S.; Bare, S. R.; Cargnello, M. *J. Am. Chem. Soc.* **2018**, *140*, 12930.

(71) Stern, E., EXAFS theory. In *X-ray absorption: principles, applications, techniques of EXAFS, SEXAFS, and XANES*; Koningsberger, D., Prins, R., Eds.; John Wiley and Sons: New York, 1988; p 3.

(72) Li, Y.; Zakharov, D.; Zhao, S.; Tappero, R.; Jung, U.; Elsen, A.; Baumann, P.; Nuzzo, R. G.; Stach, E. A.; Frenkel, A. I. *Nat. Commun.* **2015**, *6*, 7583.

(73) Peng, S.; Lee, Y.; Wang, C.; Yin, H.; Dai, S.; Sun, S. *Nano Res.* **2008**, *1* (3), 229−234.

(74) Shirman, T.; Lattimer, J.; Luneau, M.; Shirman, E.; Reece, C.; Aizenberg, M.; Madix, R. J.; Aizenberg, J.; Friend, C. M. *Chem. - Eur. J.* **2018**, *24* (8), 1833−1837.

(75) Rabe, P.; Tolkiehn, G.; Werner, A. *J. Phys. C: Solid State Phys.* **1979**, *12* (5), 899.

(76) McKale, A.; Veal, B.; Paulikas, A.; Chan, S.-K.; Knapp, G. *Phys. Rev. B: Condens. Matter Mater. Phys.* **1988**, *38* (15), 10919.

(77) Timoshenko, J.; Lu, D.; Lin, Y.; Frenkel, A. I. *J. Phys. Chem. Lett.* **2017**, *8* (20), 5091−5098.

(78) LeCun, Y.; Bengio, Y.; Hinton, G. *Nature* **2015**, *521* (7553), 436.

(79) Sanchez, S. I.; Menard, L. D.; Bram, A.; Kang, J. H.; Small, M. W.; Nuzzo, R. G.; Frenkel, A. I. *J. Am. Chem. Soc.* **2009**, *131* (20), 7040−7054.

(80) Timoshenko, J.; Kuzmin, A. *Comput. Phys. Commun.* **2009**, *180* (6), 920−925.

(81) Funke, H.; Scheinost, A.; Chukalina, M. *Phys. Rev. B: Condens. Matter Mater. Phys.* **2005**, *71* (9), 094110.

(82) Price, S. W.; Zonias, N.; Skylaris, C.-K.; Hyde, T. I.; Ravel, B.; Russell, A. E. *Phys. Rev. B: Condens. Matter Mater. Phys.* **2012**, *85* (7), 075439.

(83) Prasai, B.; Wilson, A.; Wiley, B.; Ren, Y.; Petkov, V. *Nanoscale* **2015**, *7* (42), 17902−17922.

(84) Frenkel, A.; Machavariani, V. S.; Rubshtein, A.; Rosenberg, Y.; Voronel, A.; Stern, E. *Phys. Rev. B: Condens. Matter Mater. Phys.* **2000**, *62* (14), 9364.

(85) Guesmi, H.; Louis, C.; Delannoy, L. *Chem. Phys. Lett.* **2011**, *503* (1−3), 97−100.

(86) García-Mota, M.; López, N. *Phys. Rev. B: Condens. Matter Mater. Phys.* **2010**, *82* (7), 075411.

(87) Soto-Verdugo, V.; Metiu, H. *Surf. Sci.* **2007**, *601* (23), 5332−5339.

(88) Delannoy, L.; Giorgio, S.; Mattei, J. G.; Henry, C. R.; El Kolli, N.; Méthivier, C.; Louis, C. *ChemCatChem* **2013**, *5* (9), 2707−2716.

(89) Kim, H. Y.; Henkelman, G. *ACS Catal.* **2013**, *3* (11), 2541−2546.

(90) Maire, G.; Hilaire, L.; Legare, P.; Gault, F.; O'cinneide, A. *J. Catal.* **1976**, *44* (2), 293−299.

(91) Varvenne, C.; Luque, A.; Nöhring, W. G.; Curtin, W. A. *Phys. Rev. B: Condens. Matter Mater. Phys.* **2016**, *93* (10), 104201.

(92) Nöhring, W. G.; Curtin, W. A. *Modell. Simul. Mater. Sci. Eng.* **2016**, *24* (4), 045017.

(93) Petkov, V.; Prasai, B.; Shastri, S.; Park, H.-U.; Kwon, Y.-U.; Skumryev, V. *Nanoscale* **2017**, *9* (40), 15505−15514.